The Evolving Structure of an Upwelling Filament

PIERRE FLAMENT, LAURENCE ARMI, AND LIBE WASHBURN

Scripps Institution of Oceanography, University of California San Diego, La Jolla

The evolution of an upwelling filament was studied over a 2-week period by using satellite infrared images, and its thermohaline structure was mapped in situ. The surface velocity field consisted of a large meander extending offshore for at least 300 km. The northern branch was ~40 km wide, flowing offshore at a peak velocity of 0.55 m/s; the southern branch was flowing inshore at 0.35 m/s. The offshore transport was more than 10^6 m^3 s^{-1}, larger than the Ekman transport. The meander was unstable to barotropic instabilities at a scale of ~15 km. From a succession of images a surface convergence $\gamma \approx 8 \cdot 10^{-6}$ s^{-1} over 20 km was observed near the sharp front limiting the filament to the south. The ~350 m width of the front indicates a separation of scales between the large-scale strain field and the mixed-layer turbulence parameterized with an eddy diffusion coefficient $K_H \approx 0.25$ m^2 s^{-1}. Thermohaline layers that originated at the convergence near the sharp front suggest a secondary circulation subducting denser waters to the south underneath the lighter northern water.

1. INTRODUCTION

Upwelling filaments are narrow jets that originate on the California shelf and advect cold coastal water several hundreds of kilometers offshore [*Brink*, 1983]. These features have also been referred to as tongues, plumes, or squirts; we will use the term upwelling filament, which describes their shape and their connection to the coastal upwelling region as seen from the satellite images and has been used frequently in the recent literature. Figure 1 is a satellite infrared image from June 1981 in which at least six filaments are seen between Cape Mendocino and Point Conception. They lie in deep water, west of the continental slope, shown by the 300-m and 3000-m isobaths. Time sequences of images show that their structure varies on a time scale of a few days.

The objectives of the experiment reported here were to map the thermohaline structure of a filament rooted near Point Arena and to study the associated mixing processes. This is, in effect, a flow visualization experiment: the cold upwelled water will be shown to provide a dye tracing the large-scale flow on the satellite images. The images retransmitted in real time to the ship were used to select the track along which the jet was surveyed. The survey consisted of closely sampled hydrographic sections ("tow-yo" sections) and continuous measurement of surface salinity and temperature while the ship was underway. We will show that small-scale frontal structures have a distribution given primarily by the large-scale strain field, which can be inferred from the satellite images. Although the California Current was chosen for operational reasons, our conclusions should be general, and a study of this type should be applicable to other coherent flow structures as well.

2. DESCRIPTION OF THE EXPERIMENT

The survey was conducted aboard the R. V. *Wecoma* in July 1982 during the Coastal Ocean Dynamics Experiment (CODE 2), leg 9. Figure 2 shows the area studied along with the cold filament rooted near 124°30′W, 38°30′N, meandering westward to 127°00′W, 38°00′N. Figure 3 summarizes the schedule of the experiment.

From July 8 to 17 the surface winds were ~10 m/s from the northwest, in response to a high centered at 150°W, 40°N and

a trough over the continent. Clear satellite images were acquired on July 8, 9, 15 and 16. From July 17 to 21 the pressure gradient weakened in response to a low centered at 130°W, 30°N. The variable winds were less than 2 m/s, and the sky was overcast. On July 21 a cold front swept the area, the wind veered to the NNW and increased to 10 m/s. Three satellite images were acquired on July 22 and 23, and the survey of the filament was started.

The survey lasted 4 days, from July 23 to 26. The ship track during the survey is shown on Figure 2. The tow-yo section of the jet was made on July 24 from 0000 UT to 0600 UT, some 25 hours after the last clear image. After the tow-yo section, *Huyer et al.* [1984] made 20 conventional stations on either side of the filament. *Kosro* [1985] collected Doppler acoustic velocimeter profiles during the entire cruise.

Section 3 decribes the sequence of satellite images, section 4 the different surface water types, and section 5 the subsurface thermohaline strucuture of the filament. The observations are summarized and discussed in section 6. Details concerning the instruments used and the data processing are found in the appendix.

3. SEQUENCES OF SATELLITE IMAGES AND INFERRED FLOW

The evolution of the filament over the 2 weeks of the experiment is shown in Figure 4(a, b, c). These images are separated by about 1 week in time, which is comparable to the time of advection across an image and exceeds the lifetime of most small eddies—hence small-scale features have little resemblance among these images. Successive images separated by half a day in time are well correlated, and the evolution of small eddies can be followed in a such sequence. Figures 5 and 6 show two sequences of three images ending on Figures 4b and 4c, respectively. These images have been enlarged and enhanced by whitening their spectral density to emphasize small features [cf. *Armi and Flament*, 1985].

The shape of the large filament rooted near Point Arena evolved significantly over 2 weeks:

On July 9 (Figure 4a) it consists of a regular band of cold water 20 km wide that originates near 124°W, 39°N and extends southwestward to 126°W, 38°N; the region of cold water near the coast is narrow ~30 km.

On July 15 (Figure 4b) the root of the filament has thickened to about 50 km; stronger curvature and meanders are seen, and some frontal waves are present on the southern boundary near 125°W.
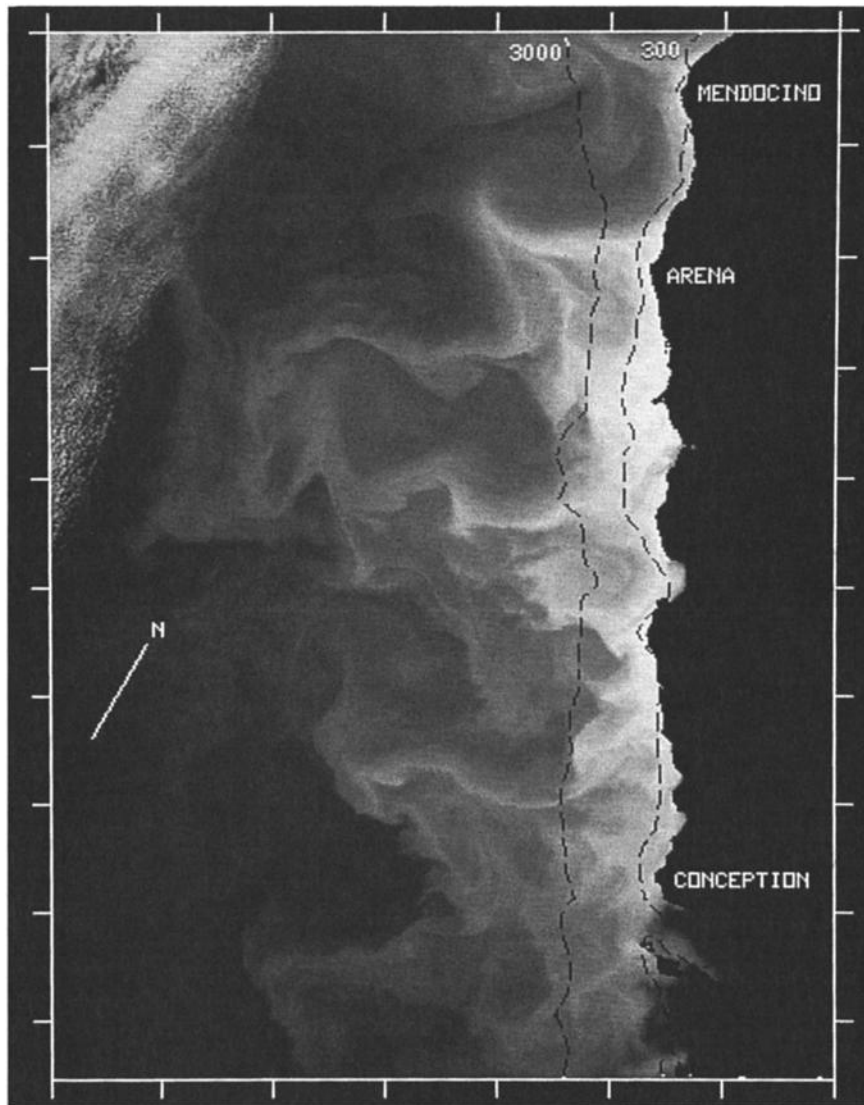
Fig. 1. A satellite infrared image of the California Current taken on June 15, 1981, at 0400 UT. Light gray shades correspond to cold water. The spacing of the tic marks is 100 km. Cold upwelled water is seen on the continental shelf and slope shown by the 300-m and 3000-m isobaths (dashed lines). Several upwelling filaments are present between Cape Mendocino (124°20'W, 40°20'N) and Point Conception (120°30'W, 34°30'N).

On July 22 (Figure 4c), after 4 days of slack wind, the shape has changed dramatically: the cold filament has broken into distinct patches of cold water (breaks are seen near 125°20'W, 38°40'N and 126°30'W, 38°00'N), frontal instabilities have grown, and eddies are shed along the southern boundary. The cold coastal region has widened to more than 50 km, and the root has moved southward to 38°30'N.

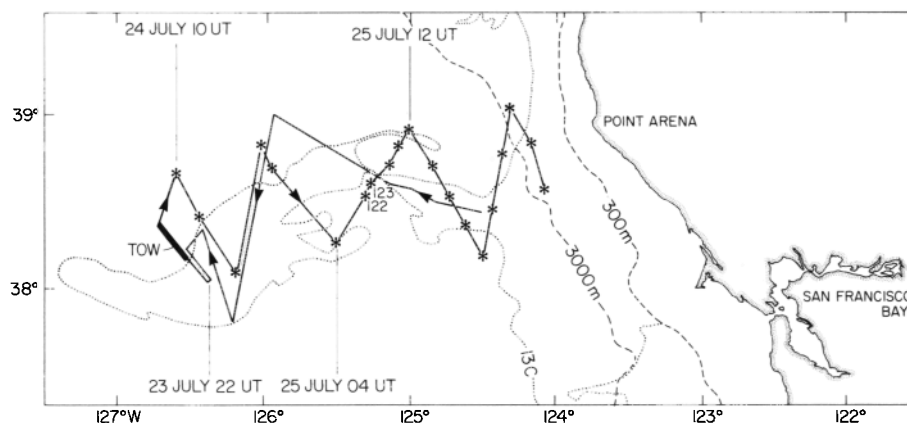A second filament flowing southward is seen in the south-

Fig. 2. Area studied. Shown are the ship track over ground during the entire survey (solid line), the absolute position of the tow-yo hydrographic section (thick line), and the 300-m and 3000-m isobaths (dashed lines). The position of the filament on July 22, 1982, at 2300 UT is outlined by the 13°C isotherm (dotted line). The hydrographic stations of *Huyer et al.* [1984] are marked with stars.
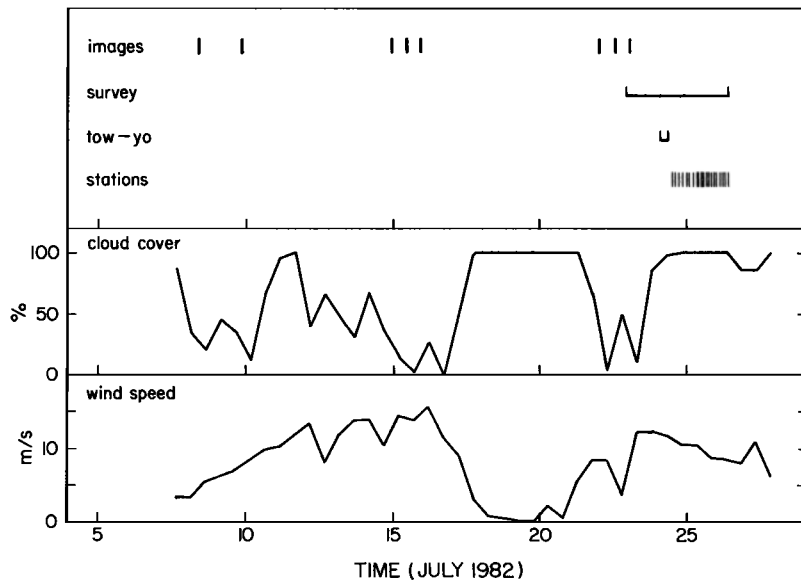
Fig. 3. Schedule of the experiment. Times of collection of cloudless images, of the underway survey of the filament, of the tow-yo section, and of the hydrographic stations of *Huyer et al.* [1984]. Time series of cloud cover and wind speed from the log of the R. V. *Wecoma*.
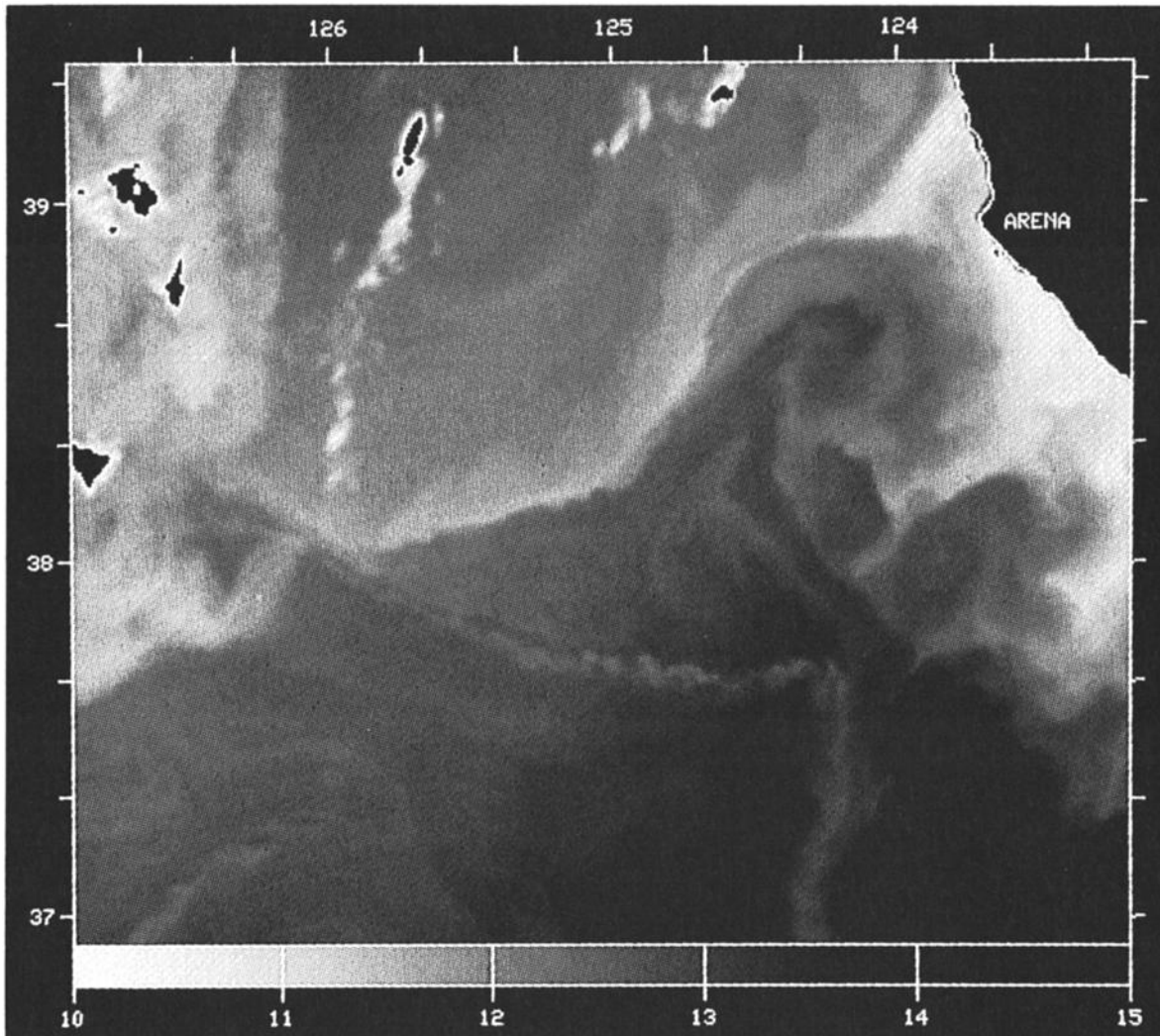
Fig. 4a

Fig. 4. Three calibrated satellite infrared images from the satellite NOAA 7 spaced about 1 week in time. Light gray shades correspond to cold water; the calibration wedge is in Celsius: (a) July 9, 2200 UT; (b) July 15, 2300 UT; (c) July 22, 2300 UT. The complete sequences ending on (b) and (c) are presented in Figure 5 and Figure 6 for the offshore portion of the images.
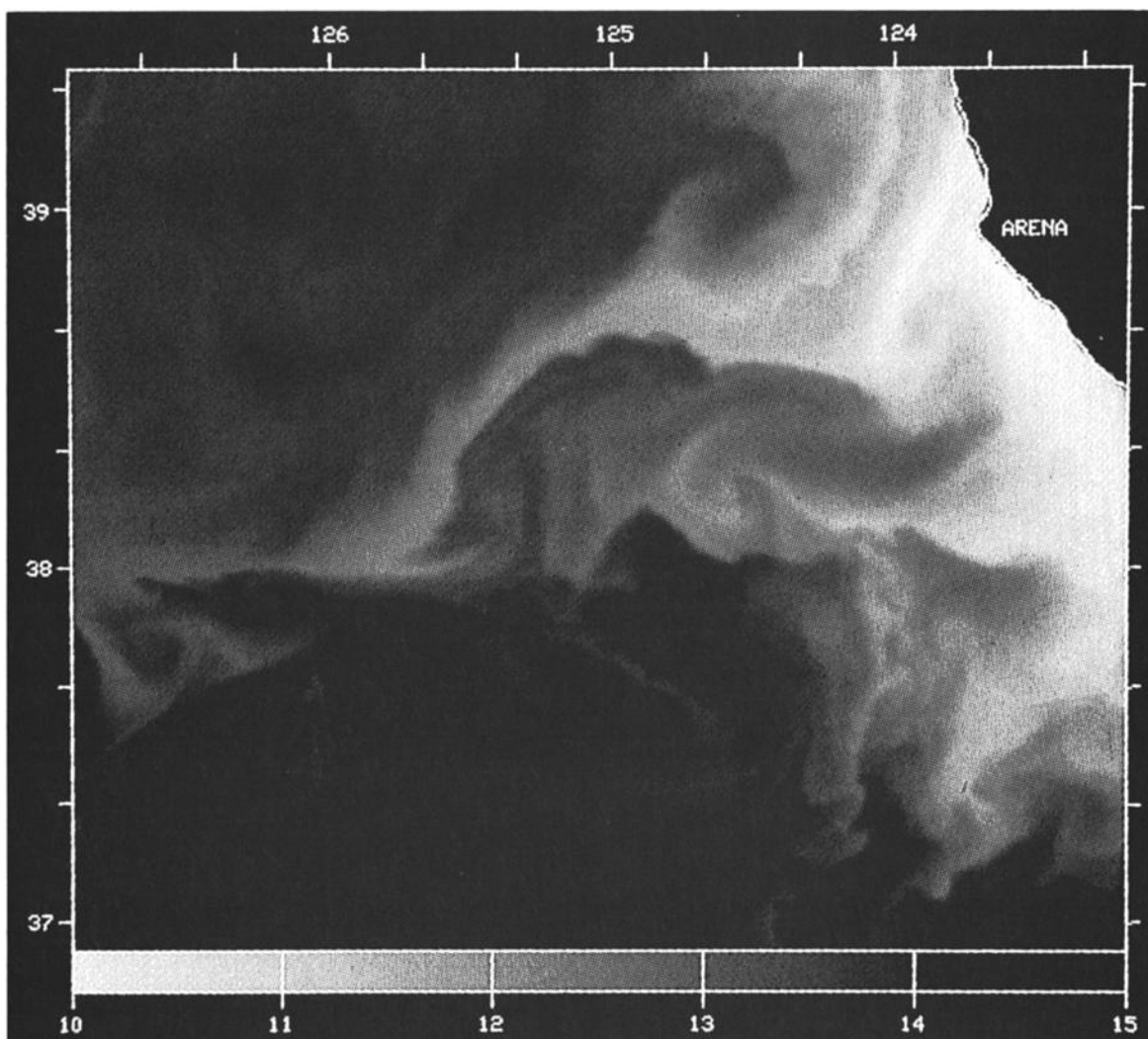
Fig. 4b

eastern corner of the images. A smaller filament is also seen growing near 124°00'W, 38°20'N. On Figure 4a it consists of a small protrusion of cold water south of Point Arena. On Figure 4b it has grown westward to 125°W. On Figure 4c it has disappeared, possibly by merging with the larger one to the north or to the south.

The boundaries of the filament are not symmetric. To the south the cold water is limited by a sharp front less than 1 km wide (the pixel size), whereas to the north the transition from cold to warm water takes place gradually over ~20 km. The sharp front coincides with the line along which cyclonic instabilities occur. This asymmetry, observed in all the images, will be discussed in detail in sections 4 and 5, using in situ data.

A convergence of surface isotherms can be seen south of the filament in the sequence shown in Figure 5. A narrow streak of cold water near 125°30'W, 38°00'N is advected toward the sharp southern front and eventually coalesces with it after 24 hours. Radiometric temperature sampled along the line in Figure 5 is shown as a function of latitude in Figure 7. Two bands of warm water are indicated by arrows. The distance between the southern edge of the warm band to the south (stippled) and the axis of the warm band to the north decreases from 20 km to 13 km after 12 hours and 10 km after 24 hours. Similar cross-isotherm convergences have been detected in other sequences of images.

If the cross-isotherm component of velocity has a uniform convergence of the form $v = -\gamma y$, where y is a cross-isotherm coordinate, the distance between isotherms decreases as $y = y_0 e^{-\gamma t}$. For this sequence the convergence rate is $\gamma \approx 8 \cdot 10^{-6}$ s^{-1}. This convergence is apparently spread over at least 10 km south of the filament. It does not seem to occur in the cold filament or north of it because a twofold reduction of the width of the filament is not observed in the same period. It is not possible to estimate the convergence in the along-isotherm direction, and thus we cannot tell from satellite images alone whether $\partial_y v$ is balanced by a divergence $\partial_x u$ (confluence) or is a real surface convergence with associated downwelling velocities at the base of the mixed layer.

Figure 8 shows the velocity field estimated by following features between July 21, 2300 UT and July 22, 2200 UT, overlaid on the image from July 22, 1100 UT. The features tracked are the cores of small eddies that are assumed to be advected by the large-scale flow.

The filament rooted near Point Arena corresponds to a strong offshore jet about 50 km wide with speeds up to 0.55 m/s. The offshore flow extends into the warm water north of the cold filament. South of the filament, there is a return flow about 30 km wide with 0.35 m/s onshore velocity. The complete flow pattern appears as large meander, the offshore flow entraining cold coastal water, and the weaker return flow bringing slightly warmer water inshore. The offshore and the return flows are separated by an intermediate region along
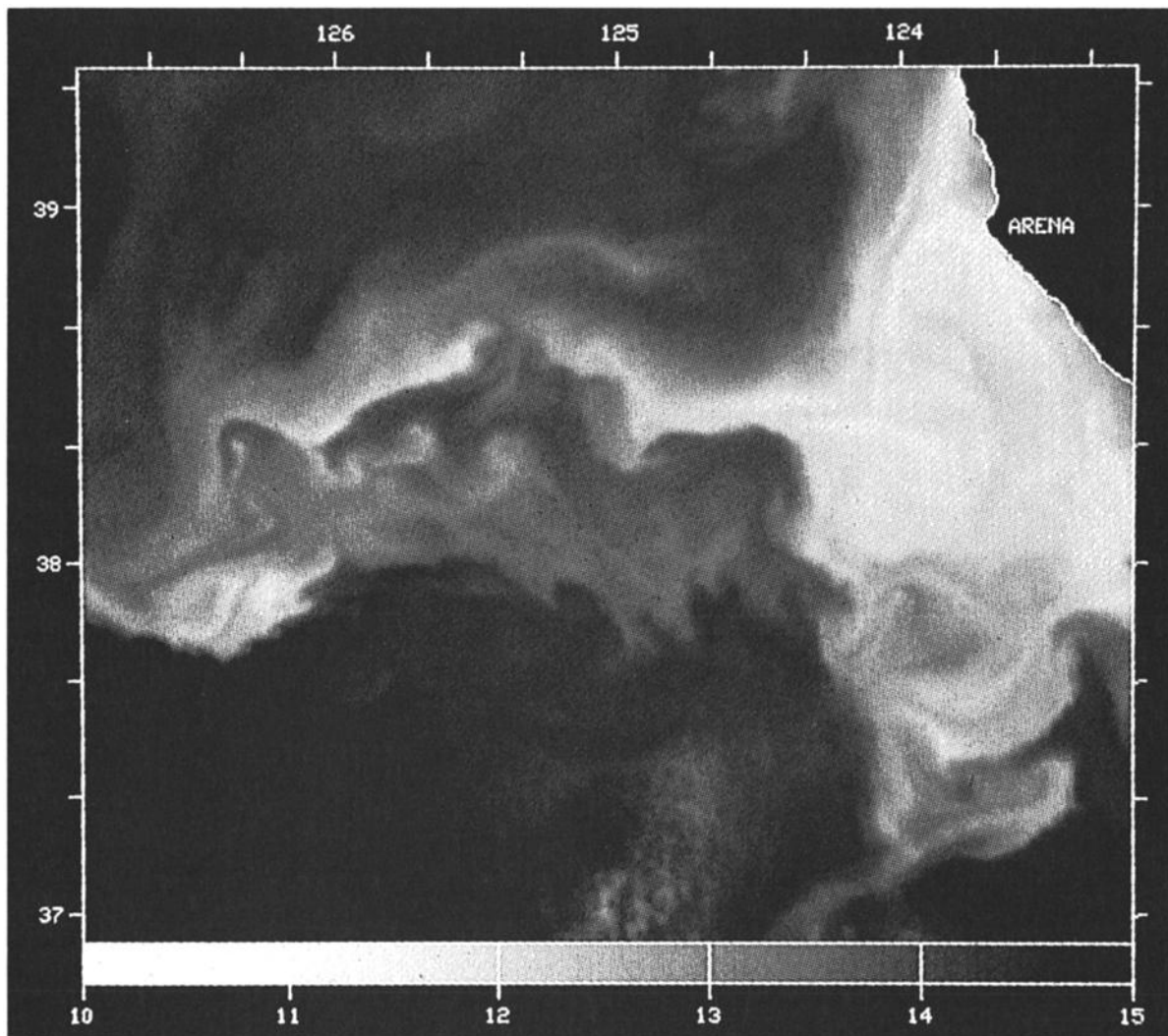
Fig. 4c

latitude 38°10'N where speeds are less than 5 cm/s. The horizontal shear between the axis of the jet and the axis of the return flow is $\sim 0.1 f$ over a scale of 80 km.

A meaningful point-by-point comparison of this velocity field with the Doppler log results of *Kosro* [1985] is difficult because the in situ survey was conducted 1-4 days after the satellite sequence, and the flow has been shown to evolve significantly over such a period. The mean and maximum speeds from the satellite images (63 samples) are 0.24 and 0.55 m/s, whereas the mean and maximum speeds at 28 m depth from the 5-min-averaged Doppler log data over the same area (705 samples) are 0.36 and 0.84 m/s. These Doppler log speeds are larger by a factor ~ 1.5. Although a real increase of the speed of the jet during the survey cannot be excluded, the discrepancy could also be a bias of satellite-derived velocities. Kosro found that the jet reaches its maximum velocity not at the sharp southern front but within the gradual northern boundary. Since most of the features that can be tracked occur near the sharp front, the satellite-derived field will systematically undersample the maximum velocity region.

The hydrographic survey of *Huyer et al.* [1984] indicates that the flow is surface intensified. Figure 9 shows a profile of geostrophic velocity referenced to 500 dbar between station 122 and station 123, spaced 8 km apart near the axis of the jet (cf. Figure 2). At the surface the velocity is about 0.5 m/s; it has been divided by e at a depth of ~ 140 m.

Instabilities are seen in Figure 6 at the southern edge of the jet and at the northern edge of the return flow. For example, near 126°15'W, 38°30'N, two small cyclonic eddies develop and pair. The line joining the cores rotates at $\sim 65°$ per day, or $0.15f$; the cores themselves presumably have a faster rate of rotation. Small eddies are also seen in the return flow near 125°15'W, 38°00'N and 126°30'W, 37°45'W. The presence of cyclonic eddies at a scale of 10-15 km rather than at the scale of the distance between the offshore jet and the return flow (80 km) suggests that the horizontal shear is not spread uniformly over 80 km but is concentrated in two narrow regions about 15 km wide on either side of the intermediate region. The horizontal temperature gradients are too small to the north of the jet to allow the recognition of similar instabilities there.

4. SURFACE WATERS

The measurements made while the ship was underway complement the satellite images by providing a better resolved surface temperature (300 m at full speed and 60 m while towing the CTD), from which we will estimate the horizontal scale of the fronts, and by concurrently providing salinity and density, from which we will infer the origin of surface waters.

The surface temperature along the westernmost cut through the jet is shown as a function of latitude in Figure 10a. The asymmetry referred to in section 3 is clearly visible. North of the filament, a temperature change of 1°C is spread over 20
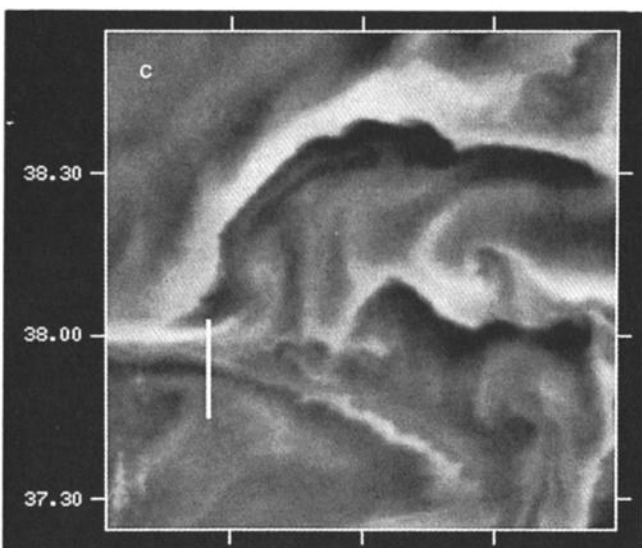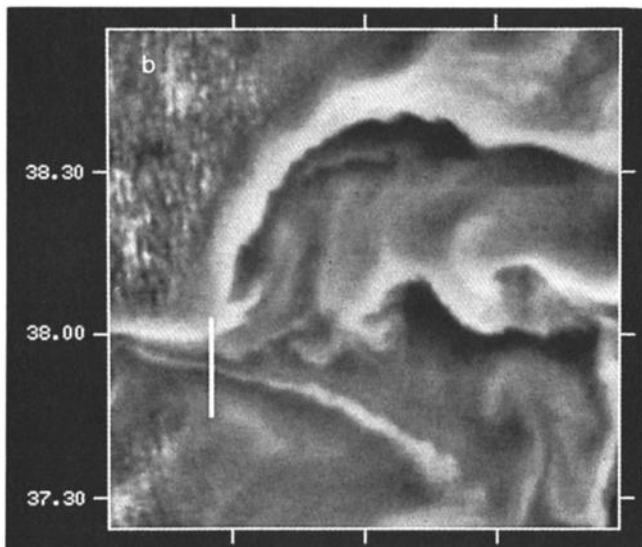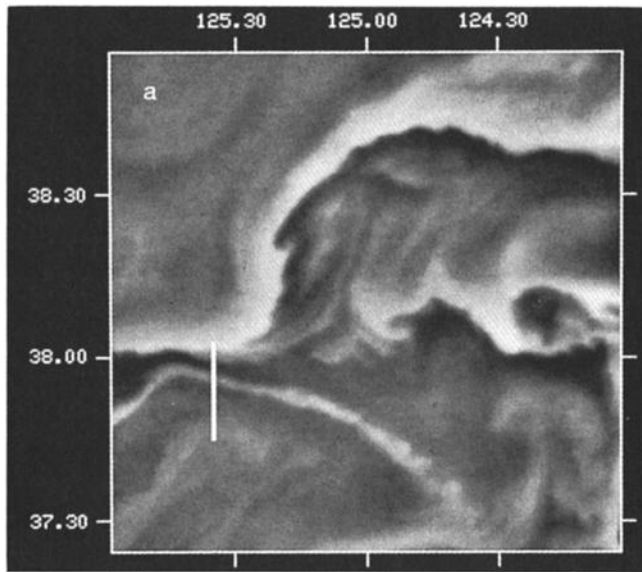
Fig. 5. The sequence of images ending on Figure 4b, enlarged and enhanced to show a region of convergence: (a) July 14, 2300 UT; (b) July 15, 1100 UT; and (c) July 15, 2300 UT. Temperature sampled along the N-S line at 125°30'W is shown in Figure 7.
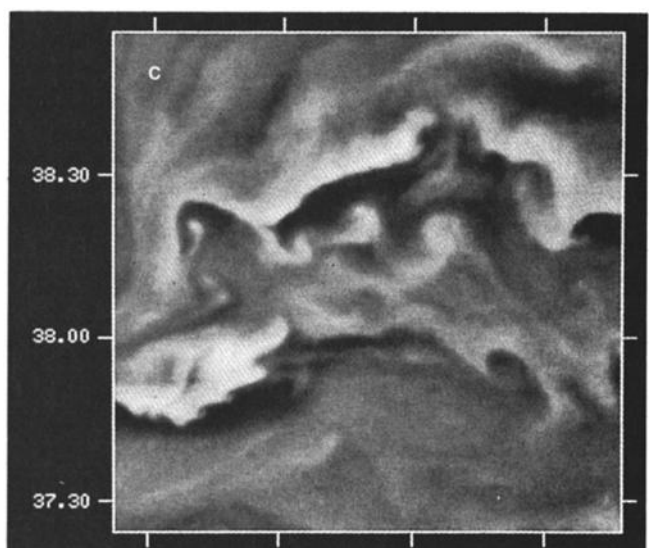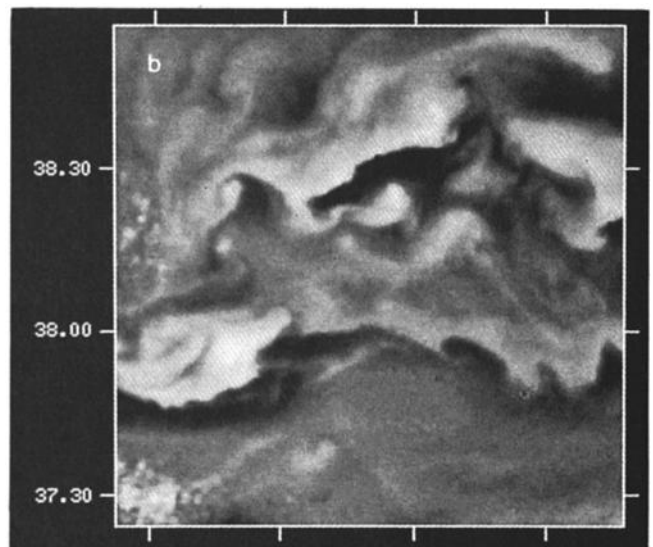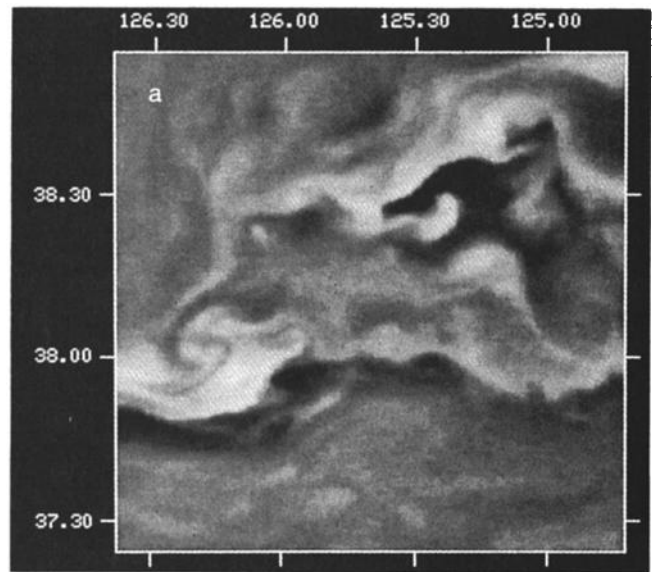
Fig. 6. The sequence of images ending on Figure 4c, enlarged and enhanced to show shear instabilities: (a) July 21, 2300 UT; (b) July 22, 1100 UT; and (c) July 22, 2300 UT.
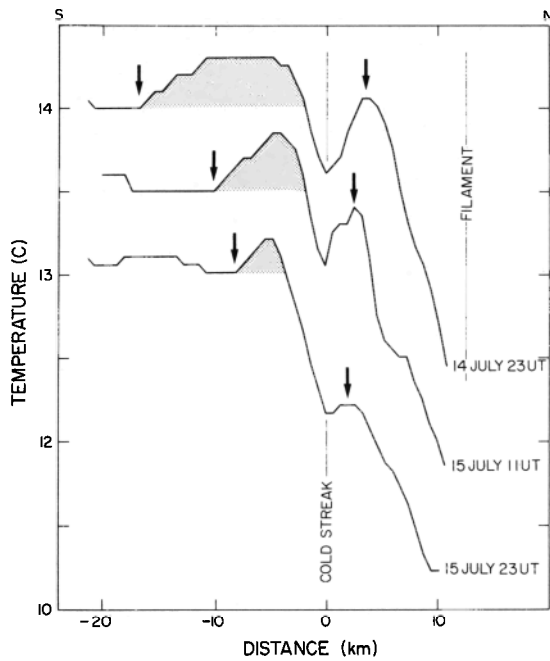
Fig. 7. Radiometric temperature as a function of latitude along the line shown on Figure 5. Two bands of warmer water are indicated by arrows, the one to the south is stippled. For clarity, successive plots are shifted 0.5°C down.

Fig. 9. Profiles of geostrophic velocity referenced to 500 dbar between station 122 at 125°18′W, 38°32′N and station 123 at 125°16.4′W, 38°36′N (cf. Figure 2). The velocity has been divided by e at a depth of ~140 m. Data from *Huyer et al.* [1984].

km. The same temperature change occurs over 350 m at the sharp front south of the filament, as seen enlarged in Figure 11.

The surface salinity and density along this cut are shown in Figure 10b and 10c. Figure 12 shows the corresponding *T-S* diagram of these surface waters. The warm water to the south of the filament is of high salinity (~33.2). The cold water and the warm water to the north are both of lower salinity
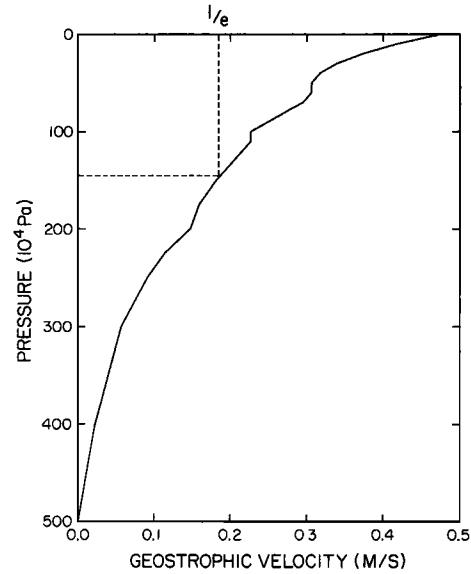
(~32.8). The sharp southern front is a transition from warm high-salinity water to colder lower-salinity water. The changes of temperature and salinity compensate each other: there is no density front. The horizontal density gradient within 1 km of the front is less than $2 \cdot 10^{-5}$ kg m^{-4} (the same temperature gradient with constant salinity would yield a density gradient of $8 \cdot 10^{-4}$ kg m^{-4}). The diffuse boundary to the north is a gradual transition from cold water to warmer water with no salinity change. There is a net surface density decrease of ~2 · 10^{-5} kg m^{-4} northward associated with the geostrophic signature of the jet.
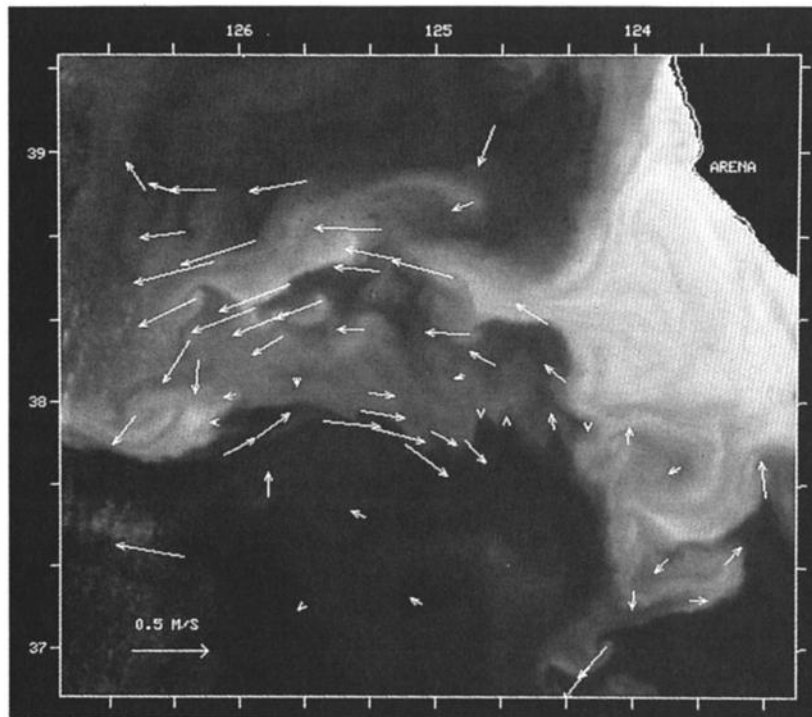

Fig. 8. Mean surface velocity field obtained by tracking thermal features between Figures 6a and 6b and between 6b and 6c overlaid on the image for July 22, 1100 UT.
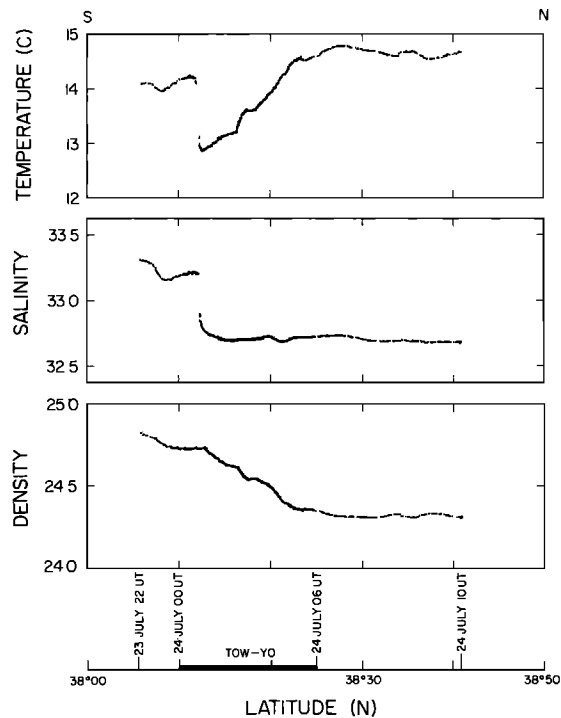
Fig. 10. Surface temperature, salinity, and density as a function of latitude along the westernmost cut through the jet (cf. Figure 2).

The cut through the filament presented here was chosen for its simplicity. Other cuts appear more complicated because, in addition to the filament, they crossed patches of water entrained in the small eddies seen in Figure 6. However, the scale of the fronts and the T-S diagrams are similar for all crossings. Figure 13 shows the temperature-salinity scatter found during the entire jet survey, the ship track for which is shown in Figure 2. Although there are considerable variations, the same pattern of three water types is observed, with sharp thermohaline fronts occurring along the 24.75 isopycnal. No significant warming of the cold filament could be detected between 124°30'W and 126°30'W.

The salinities of 13°C surface waters on the continental shelf north and south of the root of the filament are also shown in Figure 13. The surface water to the north (open circles) has
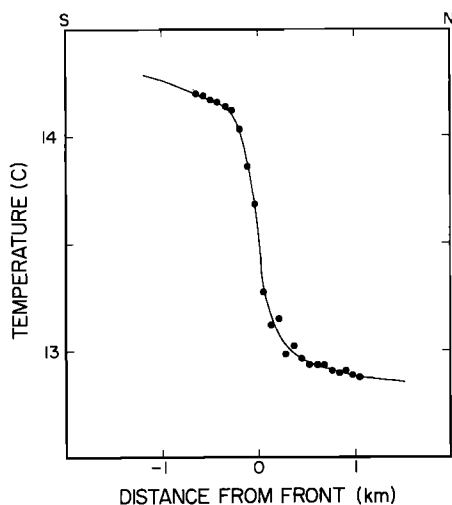

Fig. 11. Temperature as a function of distance over water at an expanded scale near the sharp front; 80% of the temperature change occurs over a distance of 350 m.
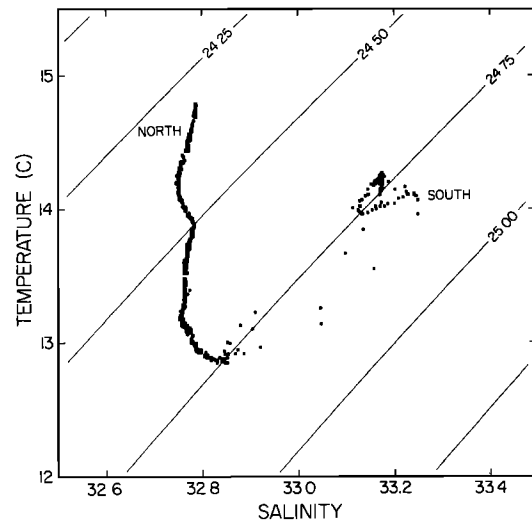

Fig. 12. Surface T-S diagram corresponding to Figure 10, showing that the sharp front is isopycnal.

T-S characteristics similar to the cold water of the filament, whereas the surface water to the south (crosses) has a salinity 0.5 higher. This suggests that the offshore flow of the meander originates on the continental shelf to the north of Point Arena (maps of near-shore water properties during CODE 2 can be found in Huyer et al. [1984]).

5. A SECTION THROUGH THE FILAMENT

The purpose of the hydrographic section was to map the subsurface thermohaline structure of the filament described above. The section, made by towing and yo-yoing a CTD (conductivity, temperature, and depth sensor) between the surface and a depth of 120 m, was started 25 hours after the last clear image shown in Figure 4c. The ship track is labeled X'Y' in Figure 14. To first order the surface water velocity in the vicinity of the tow is estimated to consist of a translation at 0.3 m/s toward 225° and a counterclockwise rotation at 65°/day (cf. Figure 6). An opposite displacement has been applied to the ship track X'Y' to find the approximate position XY of the section with respect to features observed in Figure 4c. This position is no more than indicative, since the flow probably contained strain and surface convergence and was more complicated than solid-body translation and rotation. Also, since the tow lasted 6 hours, the section is not truly synoptic.

The surface temperature field on July 22, 2300 UT is shown color coded in Plate 1a (cf. Figure 4c). (Plate 1 can be found in the separate color section in this issue.) The vertical sections of temperature, salinity, and density along XY are shown in Plates 1b, 1c and 1d. These sections are presented as color-coded images to visually enhance small thermohaline features difficult to perceive in line drawings such as shifted vertical profiles or contour plots. They are obtained by linear interpolation between successive profiles (see appendix). The path of the CTD for the first 10 yo-yo's is overlaid on Plate 1d to show the spacing between profiles. The same color coding for temperature has been used for the surface field in Plate 1a and for the vertical section in Plate 1b.

The sharp southern front is located at kilometer 3; the diffuse northern boundary of the filament is spread between kilometers 5 and 15 (Plates 1b and 1c). The cold filament visible on the satellite images is confined to the mixed layer: there is no front in the thermocline. At the scale of the section the
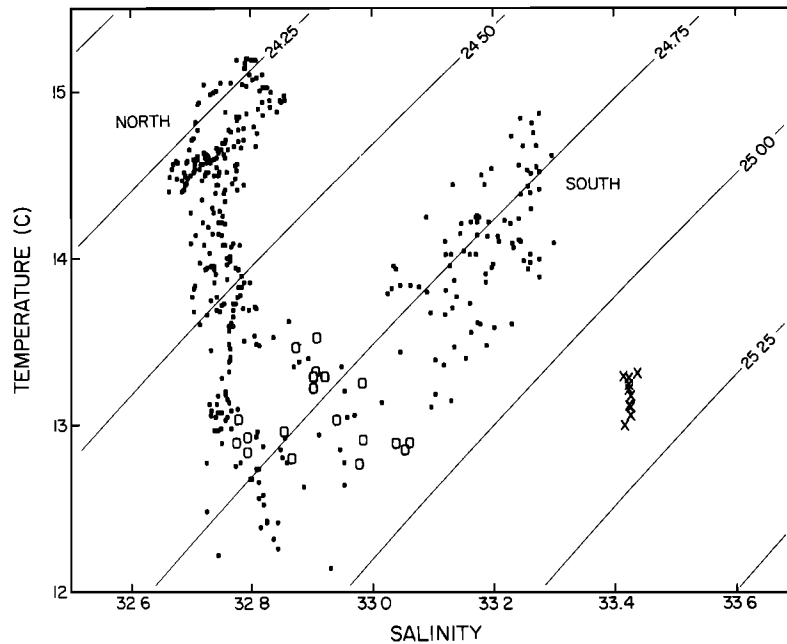
Fig. 13. Scatter plot of surface water temperature versus salinity: (dots) entire jet survey west of longitude 124°30'W; (open circles) ~13°C nearshore water at latitude 39°N on July 22; (crosses) ~13°C nearshore water at latitude 38°N on July 19.

horizontal variations of temperature at the surface and in the seasonal thermocline are not correlated. As discussed in section 4, temperature and salinity changes compensate each other at the sharp front: there is no density front in the mixed layer at kilometer 3 (Plate 1d).

Some of the shortcomings of these sections are distortions by internal waves and near-inertial shear. High-frequency internal waves displace isopycnals vertically and appear as undulations of isotherms and isohalines which may be aliased. Using density as the ordinate instead of depth to display temperature and salinity removes these distortions. For example, compare Plates 1b and 1c with 1e and 1f at kilometer 20. Low-frequency vertical shear may also advect thermohaline features in different directions at different depths. The section was made after an increase in wind, and near-inertial waves excited in the mixed layer were probably incoherent with those in the seasonal thermocline [see Davis et al., 1981, Figure 2]. A section may be noticeably different half an inertial period later.

Figure 15 shows a pair of successive downward vertical profiles of temperature ~250 m apart on either side of the front. The profile to the south has a ~33-m mixed layer, whereas the profile to the north has a shallow mixed layer less than 10 m deep, underneath which an intrusion of warmer southern water is seen (stippled). This intrusion is more saline than the cold surface water but has the same density.

A three-layer vertical structure is apparent from kilometer 7 to kilometer 17 (Plate 1b). At kilometer 10, starting at the surface, there is a 25-m-thick mixed layer of warm low-salinity northern water, a 15-m-thick layer of colder low-salinity water, a layer of warmer higher-salinity water, and finally, the normal seasonal thermocline. The cold middle layer is connected to the cold surface filament and is of constant density (Plate 1f). The warm lower layer is similarly connected to the warm water to the south of the front, and its density increases northward at a rate of $3 \cdot 10^{-5}$ kg m^{-4}.

The fact that the two deeper layers are connected to the surface suggests a subduction of the heavier surface waters

found near the front, under the lighter surface water to the north, possibly forced by a convergence in the frontal region (cf. Figure 7).

Figure 16 shows that the T-S diagrams at the surface (cf. Figure 12) and of the vertical profile at kilometer 10 are similar. The three layers near kilometer 10 have T-S characteristics resembling those of the three water types present at the surface across the jet. The lower layer at kilometer 10 is slightly colder and more saline than the water south of the front, but the difference is no larger than the T-S scatter of the southern water observed during the survey of the filament (Figure 13).

Ekman divergence resulting from the variation in local vorticity across a narrow jet could produce upwelling at the axis of the jet [Niiler, 1969]. The presence of the warm layer underneath a colder layer indicates that the cold filament is not the result of thermocline water being upwelled locally.

A similar structure is found elsewhere along the filament, as shown in Figure 17 by a pair of stations from Huyer et al. [1984]. Station 122 (dashed lines) is in the filament, while
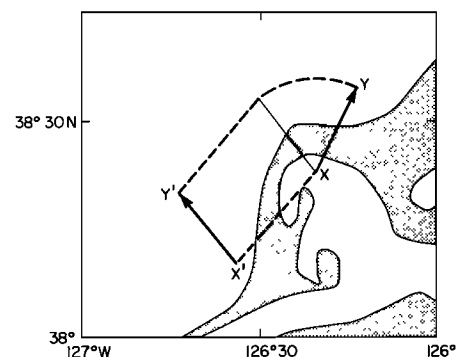

Fig. 14. Ship track over ground during the tow (X', Y'), and approximate ship track (XY) with respect to features observed on the last satellite image. XY is obtained by a 30-km translation toward 45° and a 65° clockwise rotation.
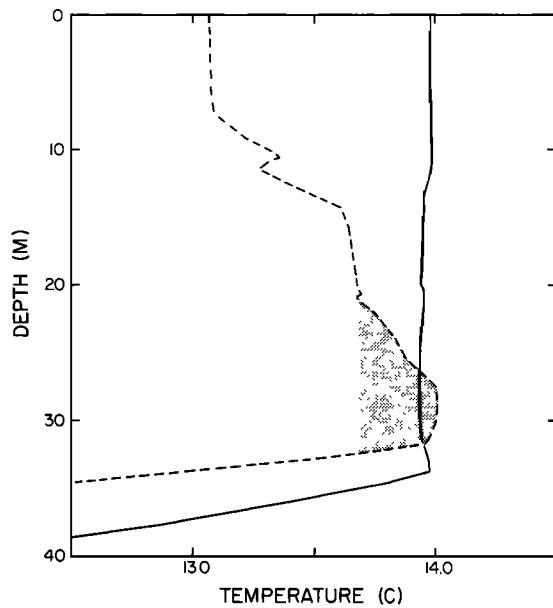
Fig. 15. A pair of vertical profiles of temperature to the south (solid line) and to the north (dashed line) of the sharp front.

station 123 (solid lines) is in the warmer region 8 km to the northeast. Two mixed layers are seen at station 123. The deeper one between 25 m and 35 m depth has T-S characteristics similar to the single surface mixed layer at station 122, as indicated by the stippled bands. Although we lack a continuous section between the two stations, this similarity in temperature and salinity again suggests that the water of the lower layer at station 123 originated at the surface somewhere in the cold region of the filament.

The sharp front at the surface has a configuration similar to the experiment of *Ruddick and Turner* [19679]: a near-vertical boundary between warm saline and colder fresher water with no horizontal density gradient at which the spontaneous formation of interleaving layers driven by double diffusion is observed in the laboratory. The application of the Ruddick

and Turner scale to this weakly stratified front yields a thickness of 600 m for the layers. Clearly, the 10-m-thick warm layer intruding northward from the front is not a geophysical analog of their laboratory experiments. The evolution of this surface front is probably dominated by mixed-layer processes rather than by double diffusion.

Several other thermohaline features can be seen in Plate 1. The largest is a warm tongue ~25 m thick that detaches from the surface layer at kilometer 17 and extends northward to where we ended the section. In this region the thermocline at a depth of 45 m does not coincide with the halocline; the tongue is located at 85 m immediately below the halocline. It lies along an isopycnal in the direction of the section. The tongue resembles the third intrusion described by *Gregg* [1980], but unlike Gregg, we lack a three-dimensional survey to infer a mechanism for the formation of this feature.

6. SUMMARY AND CONCLUSIONS

An idealization of the structure of the upwelling filament, as suggested by the observations reported above, is cartooned in Figure 18 and described below.

The surface velocity field consists of a large meander extending at least 300 km offshore and having a total north-south width of about 120 km. The northern branch is about 40 km wide, wider than the cold filament observed in the images, and flows to the west at velocities greater than ~0.5 m/s. The southern branch flows shoreward at a slower velocity ~0.35 m/s and is apparently narrower than the offshore jet to the north. The geostrophic velocity referenced to 500 dbar decreases with depth; the decrease is approximately exponential, with a typical e-folding scale of 140 m. The resulting transport of the offshore flow is of the order of 10^6 m^3 s^{-1}. The observations are insufficient to estimate the transport of the return flow.

The offshore transport can be compared with the wind-driven Ekman transport during an upwelling event. For a northwesterly wind of 10 m/s and a drag coefficient of 1.4 · 10^{-3}, the offshore Ekman transport is 2 m^2 s^{-1}. For a typical flow of 10^6 m^3 s^{-1} for each jet and an alongshore spacing of
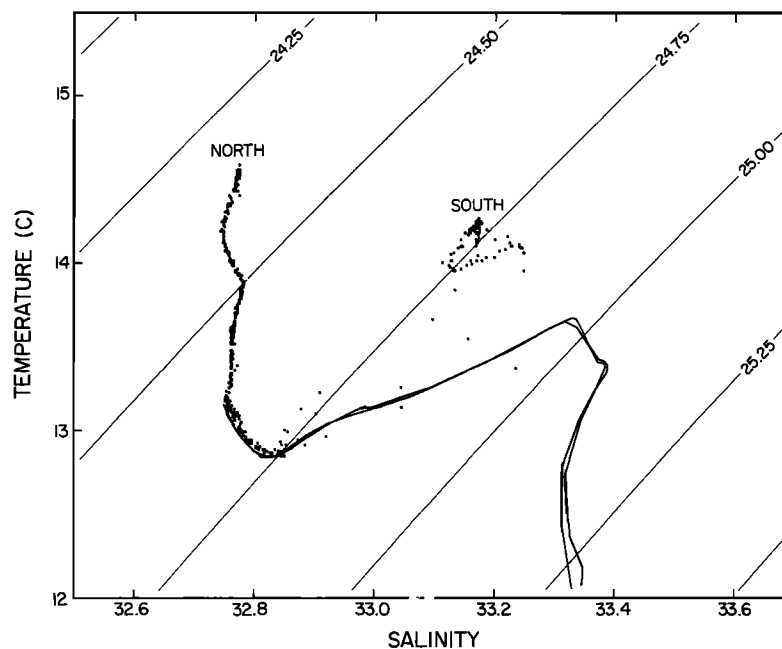

Fig. 16. T-S diagram along the tow-yo section at the surface (dots) and vertical profiles near kilometer 10 (solid line).
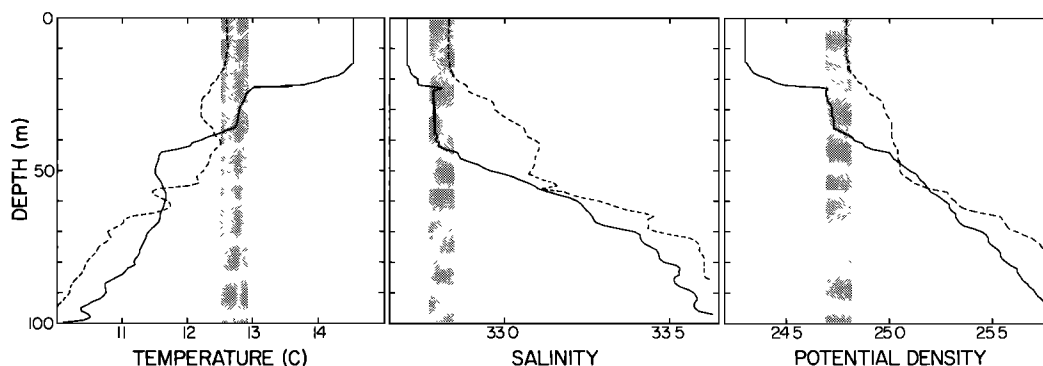
Fig. 17. Vertical profiles of temperature, salinity, and density at stations 122 and 123 (cf. Figure 2). Station 122 (dashed lines) at 125°18'W, 38°32'N is in the cold region of the jet. Station 123 (solid lines) at 125°16.4'W, 38°36'N is in the warmer region to the north. The stippled bands indicate water type similarity.

200 km between them, the offshore transport resulting from the jets is 5 m² s⁻¹. Clearly, this transport of the jets is larger than the Ekman transport.

The temperature, salinity, and density fields reflect the entrainment of cold coastal surface water by the offshore flow. The return flow brings warmer offshore water toward the coast. Three different water types are present at the surface across the filament: a high-salinity warm water to the south, the cold lower-salinity coastal water on the axis of the filament, and a warmer low-salinity water to the north. The front that delimits the filament to the south is sharp, whereas the northern boundary is gradual. The water entrained into the filament originates to the north of the root and is of the same density as the warm saline water to the south. The temperature and salinity fronts at the surface extend only to the depth of the mixed layer: the thermal features observed on the satellite image are shallower than the velocity field.

The striking lack of a density front at the temperature front observed on the satellite images may not be a general property of upwelling filaments. The same filament was surveyed at a later stage of development between August 1 and August 5, 1982, by Rienecker et al. [1985], who found that the sharp temperature front was not entirely compensated by salinity and that the cold filament was denser than the warm water to the north and to the south. Olivera et al. [1982] surveyed the nearshore part of a filament rooted south of Point Arena in July 1981. They found that the cold filament was denser than the surrounding water and that a density front was present to the north of the filament. The T-S characteristics of the filament water seem to reflect the characteristics of the source in the coastal region, which may vary in time through the up-welling season and in space along the coastline. For example, the break in the cold filament seen in Figure 4c near

125°30'W, 38°30'N may be the result of an interruption in the source of cold water during the 4 days of slack wind.

The meander is unstable along two lines where small eddies were observed: at the southern boundary of the offshore flow and at the northern boundary of the return flow. Killworth [1980] has presented a useful classification of instabilities in rotating stratified fluids for different limiting cases. The nondimensional parameters describing the instability of the flow are λ, the ratio of the horizontal length scale of the shear to the internal deformation radius, and δ, the ratio of the depth of the flow to the total depth of the ocean. In the present case, $\lambda \sim 1$ and $\delta \ll 1$, which classifies the instabilities as barotropic: it is the kinetic rather than the potential energy of the flow that feeds the growing perturbations. Another more spectacular example of these shear instabilities has been presented by Flament and Armi [1985].

These coherent eddies are an important mechanism for dissipating the kinetic energy of the jet. They create, at a geophysical scale, a horizontal mixing layer between different waters that is somewhat analogous to two-dimensional homogeneous free shear layers reviewed by Roshko [1976] but having an aspect ratio of ~500:1 as opposed to the ~1:10 aspect ratio of the laboratory experiments. It is not clear from our data what smaller-scale processes are responsible for mixing the two water types once they have been engulfed in the growing eddies. The following argument will lead us to speculate that the spiraling surface fronts are ultimately mixed at the scale of the surface mixed layer turbulence.

In secion 3 we estimated a cross-isotherm convergence rate $\gamma \approx 8 \cdot 10^{-6}$ s⁻¹, and in section 4 we gave a frontal scale of $l \approx 350$ m from underway ship measurements. A separation of scales between the strain field and diffusion that is due to small-scale turbulent motions will be assumed, and the vertical
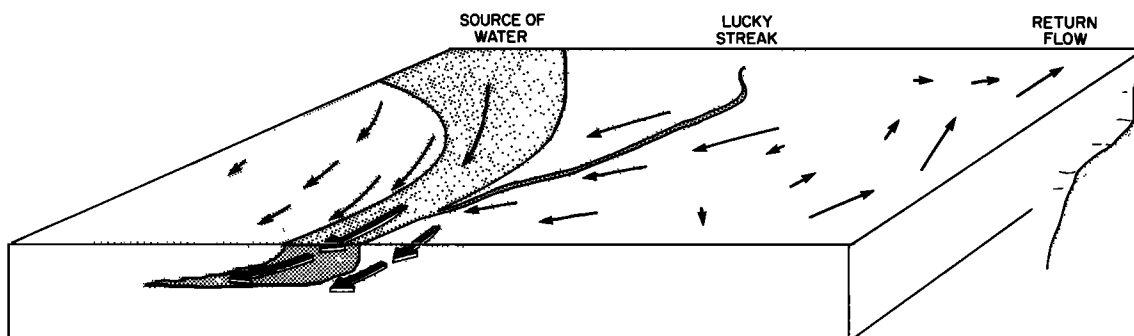

Fig. 18. A cartoon idealizing the structure of the filament.

velocity resulting from the subduction will be ignored. Assuming a steady advective-diffusive balance, we have

$$-\gamma y \frac{dT}{dy} = K_H \frac{d^2 T}{dy^2}$$

where T is the surface temperature, γ is the large-scale convergence rate, y is a cross-isotherm coordinate, and K_H is an eddy diffusion coefficient parameterizing unresolved smaller-scale turbulent motions that will be seen to be due to turbulence in the wind-mixed layer. Solutions of this equation can be found in terms of error functions; the equilibrium width of the front is [see also, *Thorpe*, 1983]

$$l = 2 \left(\frac{K_H}{\gamma} \right)^{1/2}$$

so that $K_H \approx 0.25$ m^2 s^{-1}. This is an order-of-magnitude estimate, since K_H depends quadratically on l and since we lack truly simultaneous determinations of l and γ.

Our estimate for K_H may be compared with the vertical diffusion coefficient K_v in the wind-mixed layer derived from observations of the lag of the diurnal cycle of temperature as a function of depth by *Price et al.* [1985]. Typical values are $K_v \approx 0.4$ m^2 s^{-1} for a wind speed of 8 m/s and $K_v \approx 0.1$ m^2 s^{-1} for a wind speed of 5 m/s for a spring mixed layer in the eastern North Pacific.

These values of K are close to the diffusion coefficient for a stress-driven layer, estimated by the following crude scaling argument. For most turbulent flows, $K \approx 0.3 \, u_* h$, where u_* is the friction velocity at the surface and h is the layer thickness [*Tennekes and Lumley*, 1976, Table 4.1). For $h = 30$ m and for a 10 m/s wind, $u_* = 1.4$ cm s^{-1} and $K \approx 0.1$ m^2 s^{-1}.

The order-of-magnitude agreement between K_H, inferred from the rate of convergence and from the scale of the front, and values of K_V in the mixed layer under similar wind conditions is consistent with a so-called "spectral gap" or scale separation: there is no evidence for a continuous turbulent cascade between the large-scale strain field and the mixed-layer turbulence at a scale of ~ 30 m.

The thermohaline layers that originate at the sharp front suggest a secondary circulation that subducts the heavier waters to the south underneath the lighter northern water, possibly the result of the convergence in the mixed layer. This would indicate that the cross-isotherm convergence $\partial_y v$ detected in the satellite sequence is not entirely balanced by an along-isotherm divergence $\partial_x u$, hence that $\nabla \cdot U_H \neq 0$, where U_H is the horizontal velocity field at the surface. If the subduction process begins at the root of the filament and proceeds while a parcel of water is advected at 0.5 m/s offshore, it will have taken about $3 \cdot 10^5$ s to subduct the layers seen in Plate 1. Assuming a layer thickness of 20 m and a layer extension of 15 km at this distance from the coast, the horizontal subduction velocity is 5 cm/s, so that ~ 1 m^2 s^{-1} is subducted continuously along any section. If the convergence forcing the subduction is spread over 10 km, then a downwelling velocity of 10^{-4} m/s is needed at the base of the mixed layer. For a 30-m-thick mixed layer this corresponds to a convergence of $3.5 \cdot 10^{-6}$ s^{-1}, a sizable fraction of the observed rate of convergence.

Although the subduction was observed during the summer when a strong stratification isolates the main thermocline from the surface mixed layer, one can speculate that similar processes may also occur in winter when the mixed layer is deepest and contribute intermittently to the ventilation of the thermocline. Subduction zones ~ 10 km wide, separated by

regions of ~ 200 km width that have negligible vertical motion, would result in an average downward vertical velocity of $5 \cdot 10^{-6}$ m/s, to be compared with an annual average Ekman pumping of $\sim 2 \cdot 10^{-6}$ m/s near the center of the North Pacific gyre [see, for example, *Talley*, 1985].

What forces the convergence is presently unknown. A very limited attempt to model the thermal structure of the filament has been proposed by *Flament* [1983]. The local vorticity of the jet is positive $\sim f/3$ to the south and negative to the north. This has the effect of modifying the effective Coriolis parameter across the jet and results in a convergence of the Ekman transport south of the jet, which is presumed to maintain the sharp front [see also, *Niiler*, 1969]. There are presently no observations of the in situ dynamical balance to support this model, but the frontogenesis must clearly be the result of some interaction between the large-scale flow and the dynamics of the mixed layer. *Armi and D'Asaro* [1980] postulated a similar interaction with the vorticity of the large-scale eddy field to explain the observations of interior layers detached from the benthic mixed layer.

APPENDIX: INSTRUMENTS AND DATA PROCESSING

Infrared Radiometer

The images used are from the advanced very high resolution radiometer (AVHRR) on board the NOAA 7 satellite. The AVHRR is a scanning radiometer with five spectral bands, three of which are in the thermal infrared. The spatial resolution of the AVHRR is 1.1 km at the satellite nadir. NOAA 7 is on a near-polar, sun-synchronous orbit and passes over a given point: approximately at 3 A.M. and 3 P.M. local time. A major problem in using satellites for ocean flow visualization is cloud cover: only eight images (20%) yielded usable data during the 20 days of the experiment.

The 10-μm infrared electromagnetic radiation is emitted by a skin of thickness ~ 30 μm. In the presence of a turbulent mixed layer, radiance temperature is well correlated with mixed-layer temperature, but when solar heating is strong and the wind is low, a thin warm surface layer may build up and hide the underlying temperature structure on the satellite images. The images shown in this paper were all taken under strong surface mixing conditions (~ 10 m/s winds) and are representative of the mixed layer temperature.

The digital telemetry stream was received and processed in near-real time at the Scripps Satellite Oceanographic Facility by using the software described by *Young and Fahle* [1981]. Images are corrected for earth rotation and sphericity and registered to a common mercator grid by linear interpolation. Using information from the satellite ephemeris, and the coastline as ground control points, the position accuracy is better than 2 km. The radiometer output is calibrated to Celsius by using the internal temperature references of the satellite under the assumption that the ocean surface radiates like a perfect blackbody. The rms noise of the radiometer is equivalent to 0.1°C, but the calibration neglects physical processes that contaminate the radiance temperature by errors one order of magnitude larger: absorption and reemission by atmospheric layers, reflected and scattered solar radiation, variations in the surface emissivity, and subpixel clouds.

Kelly and Davis [1985] show that, over the CODE region, most of the temperature error is described by a spatially invariant offset, that channel 4 (10.5–11.3 μm) is much less contaminated by solar radiation than channel 3 (3.5–3.9 μm) and

is a better predictor of in situ temperature, and that a two-channel (3–4) correction is not effective in reducing the errors.

We used channel 4 and corrected each of the images shown in Figure 4 by adding a constant $\gamma = \langle T_s - T_4 \rangle$ to the radiance temperature (T_s is the underway temperature taken within 3 hours of the satellite pass, and T_4 is the channel 4 of the corresponding pixel). The mean residual error is 0.3 C.

During the experiment, the images were printed on an electrostatic plotter, using a 1-mm, 8 × 8 cell half-tone generator, and transmitted to the ship through analog Xerox telecopiers, which interface easily to any radio-transceiver handset with an acoustic coupler (the resolution of standard marine facsimile transmission is too poor to reproduce the half-tone mask). We used the Applications Technology geostationary satellite (ATS) as the radio link to the ship. Since at most eight distinguishable gray tones are reproduced by this method, it is not possible to show gradients of 5°C or more over large horizontal scales as well as weak fronts of 0.2°C on the same image. To circumvent this problem, the images were enhanced by whitening their spectral density [see Armi and Flament, 1985]. The delay between the satellite passage and the reception of the image on board the ship was 1–2 hours.

Underway Thermosaligraph

A platinum resistance thermometer (PRT) was fitted to the uncontaminated seawater intake at the bow of the R. V. Wecoma 3.5 m below the waterline. Taking into account the pitching of the ship, the water was pumped at depths anywhere between 2 and 5 m. To ensure compatibility with other data collected by the CODE investigators, the PRT has been calibrated against temperature from all the CTD casts of Huyer et al. [1984] that had a well-mixed surface layer at least 10 m deep. The standard error of this calibration is 0.04°C. Bucket temperatures were poorly correlated with PRT temperatures, presumably because of diurnal heating of the upper meter.

Underway salinity was measured by a Plessey STD connected to a seawater outlet in the laboratory. We estimate the lag introduced by the piping to be a few minutes. The salinity of calibration samples were measured with a Plessey salinometer. The standard error of this calibration is 0.03.

A Trimble Loran-C was used for navigation. Kosro [1985] reports Loran-C position errors in the CODE region of less than 50 m, which is much smaller than the 2-km standard position error of the satellite images. Temperature, salinity, and position were sampled every minute.

Conductivity, Temperature, and Depth Profiler

The tow-yo section through the filament was obtained with a Neil Brown CTD mounted in a standard frame with no precaution to streamline the package or control the orientation of the sensor head. The instrument was towed at 1.2 m/s and yo-yoed between 0 and 120 m depth at a winch speed of 1.1 m/s. This gives a cycle time of 5 min and a mean horizontal resolution of 180 m. At a wire angle of 45° the estimated speed of the package through the water is 0.9 m/s during downcasts and 2.1 m/s during upcasts. Figure 19 shows depth versus time for the first part of the tow.

The CTD was equipped with a standard 3-cm Neil Brown conductivity cell and a PRT. The conductivity time series have been low passed by a one-pole filter to approximately match the PRT response. The same filter time constant $\tau = 0.25$ s has been used for upcasts and downcasts. Averages were computed at a 1-m vertical resolution. Some residual salinity spik-
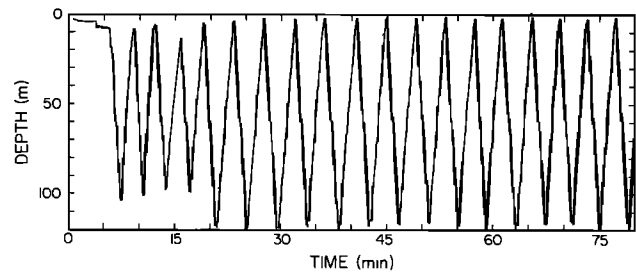

Fig. 19. Depth of the CTD versus time for the first part of the tow-yo section.

ing is still apparent on Plate 1c at kilometer 22 and at 40 m depth, where there is a thermocline and no halocline. Salinity, density, and depth were computed by using the International Equations of Seawater [Fofonoff and Millard, 1983].

The CTD was calibrated before and after the cruise at the Scripps Institution's Physical and Chemical Oceanographic Data Facility. Limited bottle data and the underway were used to check the calibration consistency.

The color-coded sections are obtained by loading two-dimensional arrays with the values of the variables along the tow path, interpolating horizontally between successive profiles (we used both up and down casts) and using a pseudo-color look-up table to display the arrays. A total of 160 profiles is used to generate Plate 1. The horizontal distance is computed by integrating the ship velocity over water from the Doppler log.

REFERENCES

Armi, L., and E. D'Asaro, Flow structure of the benthic ocean, J. Geophys. Res., 85, 469–483, 1980.

Armi, L., and P. J. Flament, Cautionary remarks on the spectral interpretation of turbulent flows, J. Geophys. Res., 90(C6), 1985.

Brink, K. H., The near-surface dynamics of coastal upwelling, Progr. Oceanogr., 12, 223–257, 1983.

Davis, R. E., R. de Szoeke, and P. P. Niiler, Variability in the upper ocean during MILE, 2, Modeling the mixed layer response, Deep Sea Res., 28A, 1453–1475, 1981.

Flament, P., Some three-dimensional aspects of coastal upwelling, in Baroclinic Instability and Ocean Fronts, Notes of the Summer Study Program in Geophysical Fluid Dynamics, Tech. Rep. WHOI-83-41, edited by M. Stern, pp. 286–297, Woods Hole Oceanographic Institution, Woods Hole, Mass., 1983.

Flament, P., and L. Armi, A series of satellite images showing the development of shear instabilities (cover blurb), Eos Trans. AGU, 66(27), 523, 1985.

Fofonoff, N. P., and R. C. Millard, Jr., Algorithms for computation of fundamental properties of seawater, UNESCO Tech. Pap. Mar. Sci., 44, 53 pp., UNESCO, Paris, 1983.

Gregg, M. C., The three-dimensional mapping of a small thermohaline intrusion, J. Phys. Oceanogr., 10, 1468–1492, 1980.

Huyer, A., J. Fleischbein, and R. Schram, Hydrographic data from the second Coastal Ocean Dynamics Experiment: R/V Wecoma, Leg 9,

6–27 July 1982, *Ref. 84-7*, Sch. of Oceanogr., Oreg. State Univ., Corvallis, 1984.

Kelly, K. A., and R. E. Davis, An analysis of errors in SST in a series of infrared images from NOAA-6, *J. Geophys. Res.*, in press, 1985.

Killworth, P. D., Barotropic and baroclinic instability in rotating stratified fluids, *Dyn. Atmos. Oceans, 4*, 143–184, 1980.

Kosro, P. M., Shipboard acoustic current profiling during the Coastal Ocean Dynamics Experiment, *SIO Ref. 85-8*, Scripps Inst. of Oceanogr., La Jolla, Calif., 1985.

Niiler, P. P., On the Ekman divergence in an oceanic jet, *J. Geophys. Res., 74*, 7048–7051, 1969.

Olivera, M., W. E. Gilert, J. Fleischbein, A. Huyer, and R. Schramm, Hydrographic data from the first Coastal Ocean Dynamics Experiment: R/V *Wecoma*, Leg 7, 1–14 July 1981, *Ref. 82-8*, Sch. of Oceanogr., Oreg. State Univ., Corvallis, 1982.

Price, J. F., R. A. Weller, and R. Pinkel, Diurnal cycling: Observations and models of the upper ocean response to diurnal heating, cooling and wind mixing, *J. Geophys. Res.*, in press, 1985.

Rienecker, M. M., C. N. Mooers, D. E. Hagan, and A. R. Robinson, A cool anomaly off Northern California: An investigation using IR imagery and in situ data, *J. Geophys. Res., 90*, 4807–4818, 1985.

Roshko, A., Structure of turbulent shear flows: A new look, *AIAA J., 14*, 1349–1357, 1976.

Ruddick, B. R., and J. S. Turner, The vertical length scale of double-diffusive intrusions, *Deep Sea Res., 26*, 903–913, 1979.

Talley, L. D., Ventilation of the subtropical North Pacific: The shallow salinity minimum, *J. Phys. Oceanogr., 15*, 633–649, 1985.

Tennekes, H., and J. L. Lumley, *A First Course in Turbulence*, The MIT Press, Cambridge, Mass., 1972.

Thorpe, S. A., Benthic observations on the Madeira abyssal plain: fronts, *J. Phys. Oceanogr., 13*, 1430–1440, 1983.

Young, T. L., and J. H. Fahle, User's manual for preliminary satellite image processing: Extraction, calibration and location, *SIO Ref. 81-36*, Scripps Inst. Oceanogr., La Jolla, Calif., 1981.

L. Armi, P. Flament, and L. Washburn, Scripps Institution of Oceanography, University of California San Diego A-030, La Jolla, CA 92093.
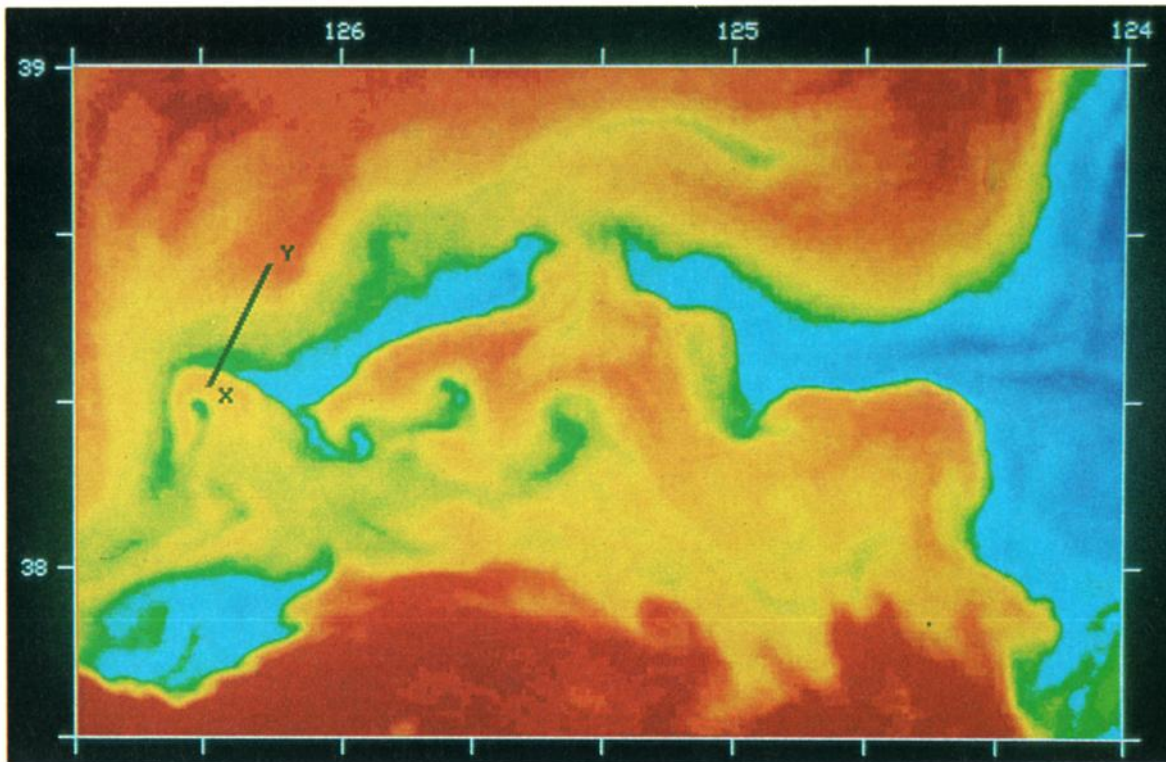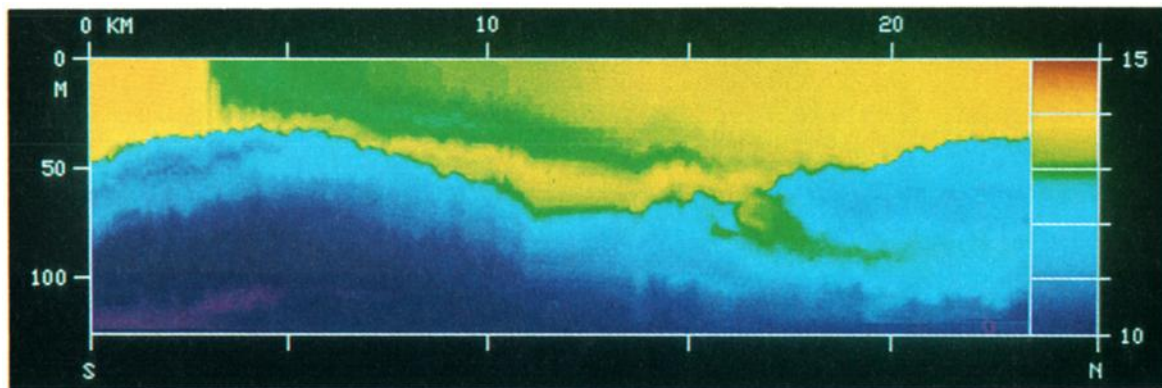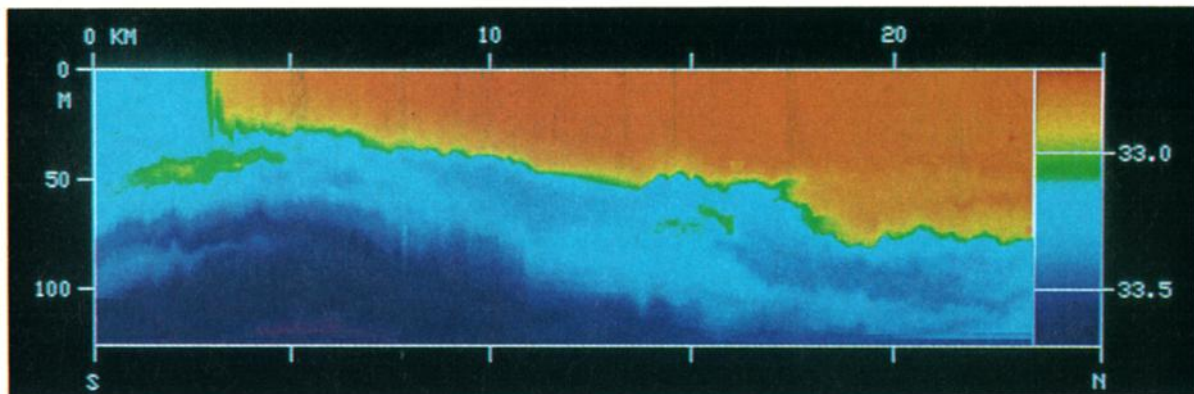
Plate 1a

Plate 1b

Plate 1c

Plate 1 [*Flament et al.*]. (*a*) Surface temperature field on July 22 at 2300 UT. The estimated track over water is XY (refer to Figure 14). Sections of (*b*) temperature, (*c*) salinity, and (*d*) density using depth as the ordinate.
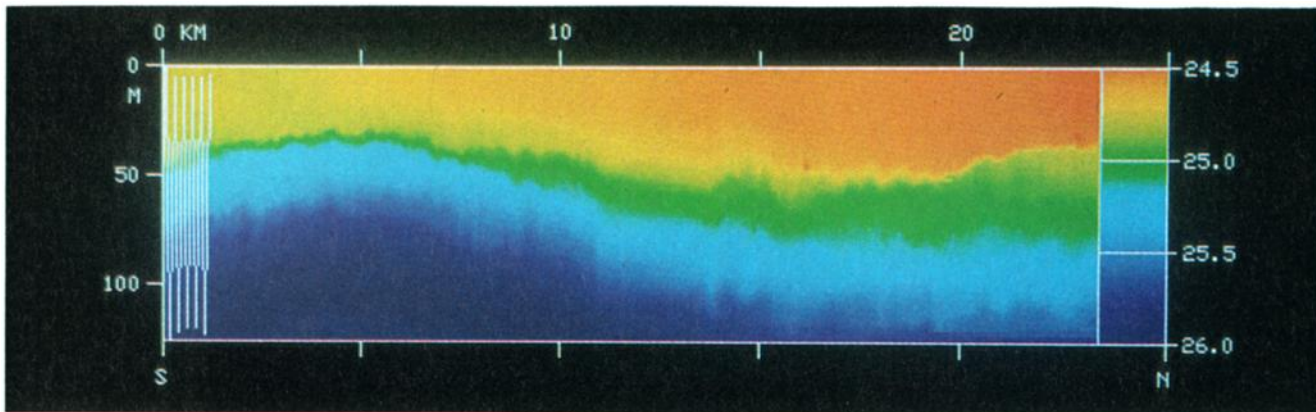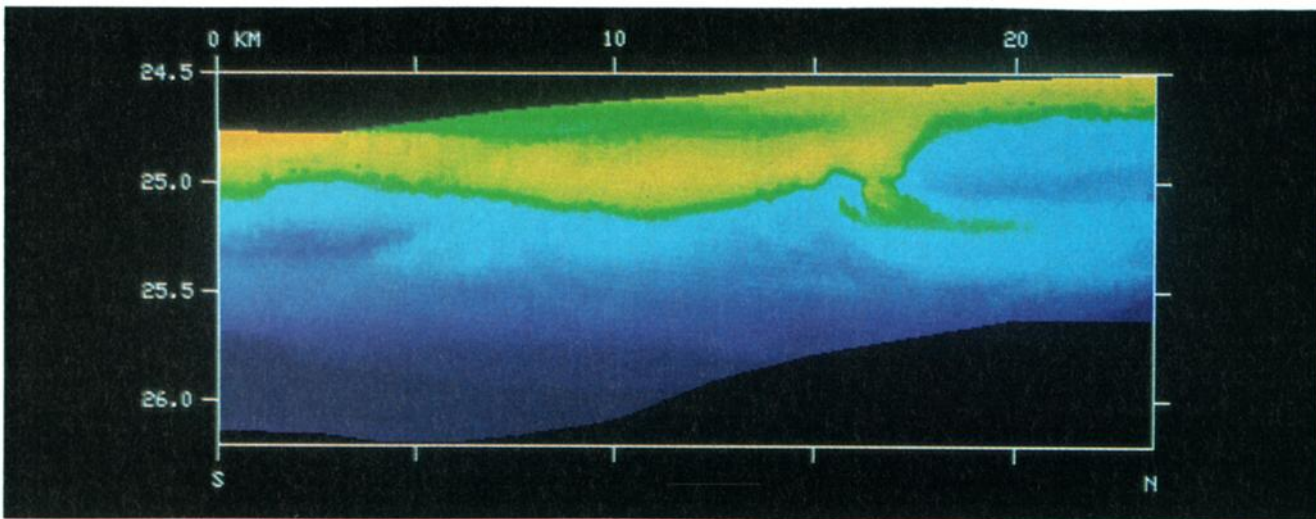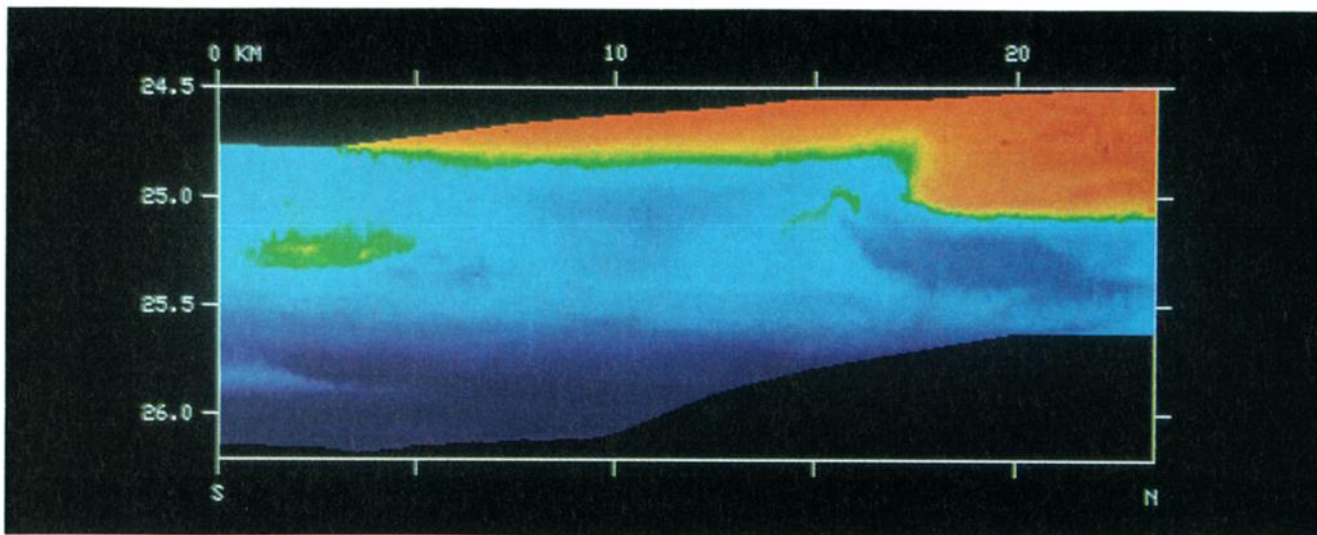
Plate 1d

Plate 1e

Plate 1f

Plate 1 [*Flament et al.*, continued]. The path of the CTD sensor during the first ten up-downs is overlaid over (d) (see also Figure 19). Sections of (e) temperature and (f) salinity using density as the ordinate.